CMS Physics Analysis Summary

Contact: cms-pag-conveners-exotica@cern.ch 2016/08/04

Search for dark matter and unparticles in events with a Z boson and missing transverse momentum in proton-proton collisions at $\sqrt{s} = 13\,\text{TeV}$

The CMS Collaboration

Abstract

A search for evidence of dark matter (DM) and unparticle production at the LHC has been performed using events containing two charged leptons, consistent with the decay of a Z boson, and large missing transverse momentum. This study is based on data collected with the CMS detector corresponding to an integrated luminosity of 2.3 fb^{-1} of pp collisions at the LHC at a center-of-mass energy of 13 TeV. No excess over the standard model expectation is observed. The results are interpreted in terms of a simplified model of DM production. For both vector and axial vector couplings between a mediator and DM particles, 95% confidence level limits are set on the observed signal strength in the plane of mediator and DM particle mass. Additionally, 90% confidence level limits are set on the DM-nucleon scattering cross section, as a function of the DM particle mass, for both spin-dependent and spin-independent coupling scenarios. In the context of an effective field theory, 95% confidence level limits are set on the DM coupling parameters to $U(1)$ and $SU(2)$ gauge fields and on the scale of new physics. Additionally, 95% confidence level limits are obtained on the unparticle model parameters.

1 Introduction

The nature of dark matter (DM) is one of the outstanding mysteries of particle physics in this new century. According to the well-established standard model of cosmology, in the total cosmic energy budget, our known matter – the ordinary particles – only occupies about 4.9%, the DM occupies 26.8%, and the rest is dark energy. Although strong astrophysical evidence indicates the existence of DM, there is no evidence yet for nongravitational interactions between DM and standard model (SM) particles. Recent DM searches have exploited a number of methods including direct detection [1] and indirect detection [2]. If there is DM that can be observed in direct detection experiments, it must have substantial coupling to nucleons, and it could be produced at the CERN LHC as well [3–17].

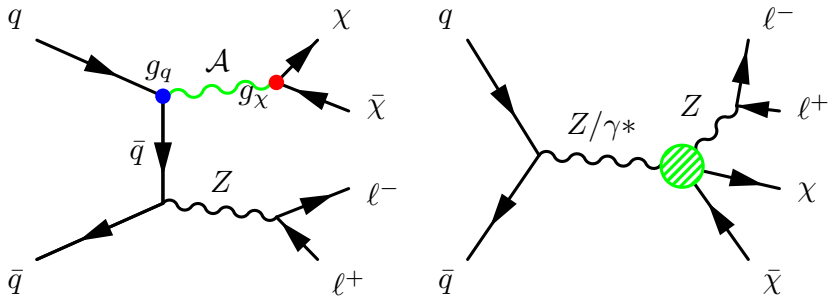

Figure 1: Feynman diagrams for production of DM pairs ($\chi\bar{\chi}$) in association with a Z boson. Left: the simplified model containing a vector mediator $\mathcal{A}$. Right: an EFT benchmark model with DM pair coupling to gauge bosons via dimension-7 operators.

The theoretically favored possibility is that DM may take the form of weakly interacting massive particles. The study presented here considers a mechanism for producing such particles at the LHC [18]. In this scenario, a Z boson, produced in proton-proton collisions, recoils against a pair of DM particles, $\chi\bar{\chi}$. The Z boson subsequently decays into two charged leptons ($\ell^+\ell^-$, where ℓ = e or μ) producing a clean dilepton signature together with missing transverse momentum due to the undetected DM particles. In this analysis, the DM particle χ is assumed to be a Dirac fermion. A simple tree-level ultraviolet-complete model [18] that contains a massive spin-1 mediator exchanged in the s-channel is considered (Fig. 1, left). In this model, the spin-1 mediator $\mathcal{A}$ could have either vector or axial-vector couplings to the SM and DM particles. The full Lagrangian of the s-channel vector-mediated DM model can be written as:

$$\mathcal{L} = \mathcal{L}_{\text{SM}} - \frac{1}{4}\mathcal{F}_{\mu\nu}\mathcal{F}^{\mu\nu} - \frac{1}{2}m_{\mathcal{A}}^2\mathcal{A}_\mu\mathcal{A}^\nu + \bar{\chi}(i\gamma^\mu\partial_\mu - m_\chi)\chi - \sum_q g_q\mathcal{A}_\mu\bar{q}\gamma^\mu(\gamma^5)q - g_\chi\mathcal{A}_\mu\bar{\chi}\gamma^\mu(\gamma^5)\chi\,,$$

where the vector mediator is labeled as $\mathcal{A}$, and its coupling to DM particles is labeled as g_χ. The coupling between the vector mediator and SM quarks is labeled as g_{q}, which is assumed to be universal to all quarks.

Another benchmark DM model containing the $\mathcal{SU}(2)_{\text{L}} \times \mathcal{U}(1)_{\text{Y}}$ gauge-invariant couplings to gauge bosons is given by an effective field theory (EFT) Lagrangian with dimension-7 operators:

$$\mathcal{L}_{\text{int}} = \frac{1}{\Lambda^3}\bar{\chi}\chi\left(\frac{c_1}{c_2}B_{\mu\nu}B^{\mu\nu} + F^i_{\mu\nu}F^{i,\mu\nu}\right)\,,$$

in which χ is the Dirac fermionic DM particle, $B_{\mu\nu}$ and $F^i_{\mu\nu}$ are the $U(1)_Y$ and $SU(2)_L$ field tensors, the parameters c_1 and c_2 are coupling constants, and Λ denotes the cutoff scale. The coupling parameters c_1 and c_2 control the relative importance of the $U(1)_Y$ and $SU(2)_L$ fields

for DM production. Any common multiplicative factor in the couplings has been absorbed into Λ. Figure 1 shows the Feynman diagrams for production of DM pairs ($\chi\bar{\chi}$) in association with a Z boson in these two types of models.

The signature for DM production considered in this analysis is the production of a pair of leptons (e^+e^- or $\mu^+\mu^-$) consistent with a Z boson, together with a large magnitude of missing transverse momentum. This same signature is sensitive to other models of physics beyond the standard model, e.g. unparticles.

The unparticle physics concept [19–22] is particularly interesting because it is based on scale invariance, which is anticipated in many beyond-the-SM physics scenarios [23–25]. The effects of the scale-invariant sector ("unparticles") appear as a noninteger number of invisible massless particles. In this scenario, the SM is extended by introducing a scale-invariant Banks–Zaks ($\mathcal{BZ}$) field, which has a nontrivial infrared fixed point [26]. This field can interact with SM particles by exchanging heavy particles with a high mass scale $M_\mathcal{U}$. Below this mass scale, the coupling is nonrenormalizable and the interaction is suppressed by powers of $M_\mathcal{U}$. The interaction Lagrangian can be expressed as:

$$\mathcal{L}_{\text{int}}^{\text{eff}} = C_\mathcal{U} \frac{\Lambda_\mathcal{U}^{d_{\mathcal{BZ}}-d_\mathcal{U}}}{M_\mathcal{U}^k} \mathcal{O}_{\text{SM}} \mathcal{O}_\mathcal{U} = \frac{\lambda}{\Lambda_\mathcal{U}^{d_\mathcal{U}}} \mathcal{O}_{\text{SM}} \mathcal{O}_\mathcal{U},$$

in which $C_\mathcal{U}$ is a normalization factor fixed by matching, $d_\mathcal{U}$ represents the possible noninteger scaling dimension of the unparticle operator $\mathcal{O}_\mathcal{U}$, $k = d_{\text{SM}} + d_{\mathcal{BZ}} - 4 > 0$ is the scaling dimension, $\Lambda_\mathcal{U}$ is the energy scale of the interaction, and the parameter $\lambda = C_\mathcal{U} \Lambda_\mathcal{U}^{d_{\mathcal{BZ}}} / M_\mathcal{U}^k$ is a measure of the coupling between SM particles and unparticles. A recent search for unparticles at CMS [17] in the same final states has shown no evidence for their existence, and this reference gives additional details of the model used. In this physics analysis summary, real emission of scalar unparticles is considered, and the scaling dimension $d_\mathcal{U} > 1$ is constrained by the unitarity condition. Figure 2 shows the tree-level diagram considered in this paper for the production of unparticles associated with a Z boson.

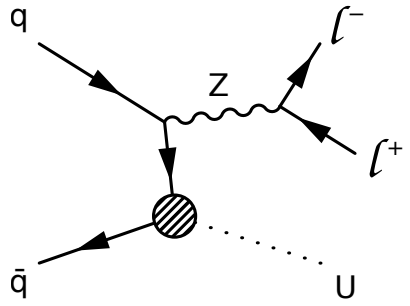

Figure 2: Feynman diagram for unparticle (denoted by $\mathcal{U}$) production in association with a Z boson. The hatched circle indicates the interaction modeled with an effective field theory operator.

The analysis is based on a data set recorded with the CMS detector in 2015, which corresponds to an integrated luminosity of $2.3 \pm 0.1\,\text{fb}^{-1}$ at a center-of-mass energy of 13 TeV. A previous CMS result [17] based on data collected at a center-of-mass energy of 8 TeV, set limits on DM interpreted through effective field theory and on unparticle production.

2 The CMS detector

The central feature of the CMS apparatus is a superconducting solenoid of 6 m internal diameter, providing a magnetic field of 3.8 T. Within the superconducting solenoid volume are a silicon pixel and strip tracker, a lead tungstate crystal electromagnetic calorimeter (ECAL), and a brass and scintillator hadron calorimeter (HCAL), each composed of a barrel and two endcap sections. Forward calorimeters extend the pseudorapidity [27] coverage provided by the barrel and endcap detectors. Muons are measured in gas-ionization detectors embedded in the steel flux-return yoke outside the solenoid. A more detailed description of the CMS detector, together with a definition of the coordinate system used and the relevant kinematic variables, can be found in Ref. [27]. Variables of particular relevance to the present analysis are the missing transverse momentum vector $\vec{p}_{\mathrm{T}}^{\,\mathrm{miss}}$ and the magnitude of this quantity, $E_{\mathrm{T}}^{\mathrm{miss}}$. The quantity $\vec{p}_{\mathrm{T}}^{\,\mathrm{miss}}$ is defined as the projection on the plane perpendicular to the beams of the negative vector sum of the momenta of all reconstructed particles in an event.

3 Simulation

Samples of simulated DM particle events are generated using MADGRAPH5_AMC@NLO [28] at leading order (LO) and matched to PYTHIA 8 [29] using tune CUETP8M1 (labeled with M for Monash) for parton showering and hadronization [30, 31]. The factorization and renormalization scales are set to $\frac{1}{2}H_T$, where H_T is the scalar sum of $\sqrt{p_T^2 + m^2}$ for all final state particles [18, 28]. The coupling g_χ is set to one. For g_q, values of 1.0 and 0.25 are considered. The signal simulation samples with $g_q = 1.0$ are processed using the detector simulation described below. Signal predictions for $g_q = 0.25$ are obtained by applying event weights based on the $E_{\mathrm{T}}^{\mathrm{miss}}$ distribution at the generator level to the fully simulated samples with $g_q = 1.0$. This procedure takes into account the non-trivial dependence of the mediator width on the coupling choice [32].

The events for the unparticle model are generated at LO with PYTHIA 8.1 [29, 33, 34] assuming a cutoff scale $\Lambda_{\mathcal{U}} = 15\,\mathrm{TeV}$, using tune 4C [35] for parton showering and hadronization. We evaluate other values of $\Lambda_{\mathcal{U}}$ by rescaling the cross sections as needed. The parameter $\Lambda_{\mathcal{U}}$ acts solely as a scaling factor for the cross section and does not influence the kinematic distributions of unparticle production [34].

The top left pane of Fig. 3 shows the distribution of $E_{\mathrm{T}}^{\mathrm{miss}}$ at the generator level for DM particles with mass 50 GeV in the simplified model. The events with larger mediator mass M_{med} tend to have a broader $E_{\mathrm{T}}^{\mathrm{miss}}$ distribution and reach further into the high-$E_{\mathrm{T}}^{\mathrm{miss}}$ regime. The analogous distribution in the dimension-7 EFT benchmark model with the DM mass $m_\chi = 1, 200, 1300$ GeV is shown in the top right pane side of Fig. 3. In the unparticle scenario, the events with larger scaling dimension $d_{\mathcal{U}}$ tend to have a a larger fraction of events in the high-$E_{\mathrm{T}}^{\mathrm{miss}}$ regime, as shown in the bottom pane of Fig. 3. The SM background $\mathrm{ZZ} \to \ell^-\ell^+\nu\bar{\nu}$ is shown as a red solid curve for a comparison in all plots.

The POWHEG 2.0 [36–40] event generator is used to produce samples of events for the $\mathrm{t\bar{t}}$, tW, $\mathrm{q\bar{q}} \to \mathrm{ZZ}$, and WZ background processes which are simulated at next-to-leading order (NLO). The $\mathrm{gg} \to \mathrm{ZZ}$ process is simulated using MCFM [41] at NLO. The Drell–Yan (DY, $\mathrm{Z}/\gamma^* \to \ell^+\ell^-$) process is generated using the MADGRAPH5_AMC@NLO event generator at LO. For all SM simulation samples, parton showering and hadronization are performed by PYTHIA 8 with tune CUETP8M1. The parton distribution set NNPDF3.0 [42] is used for all generated samples. For all Monte Carlo (MC) samples, the detector response is simulated using a detailed

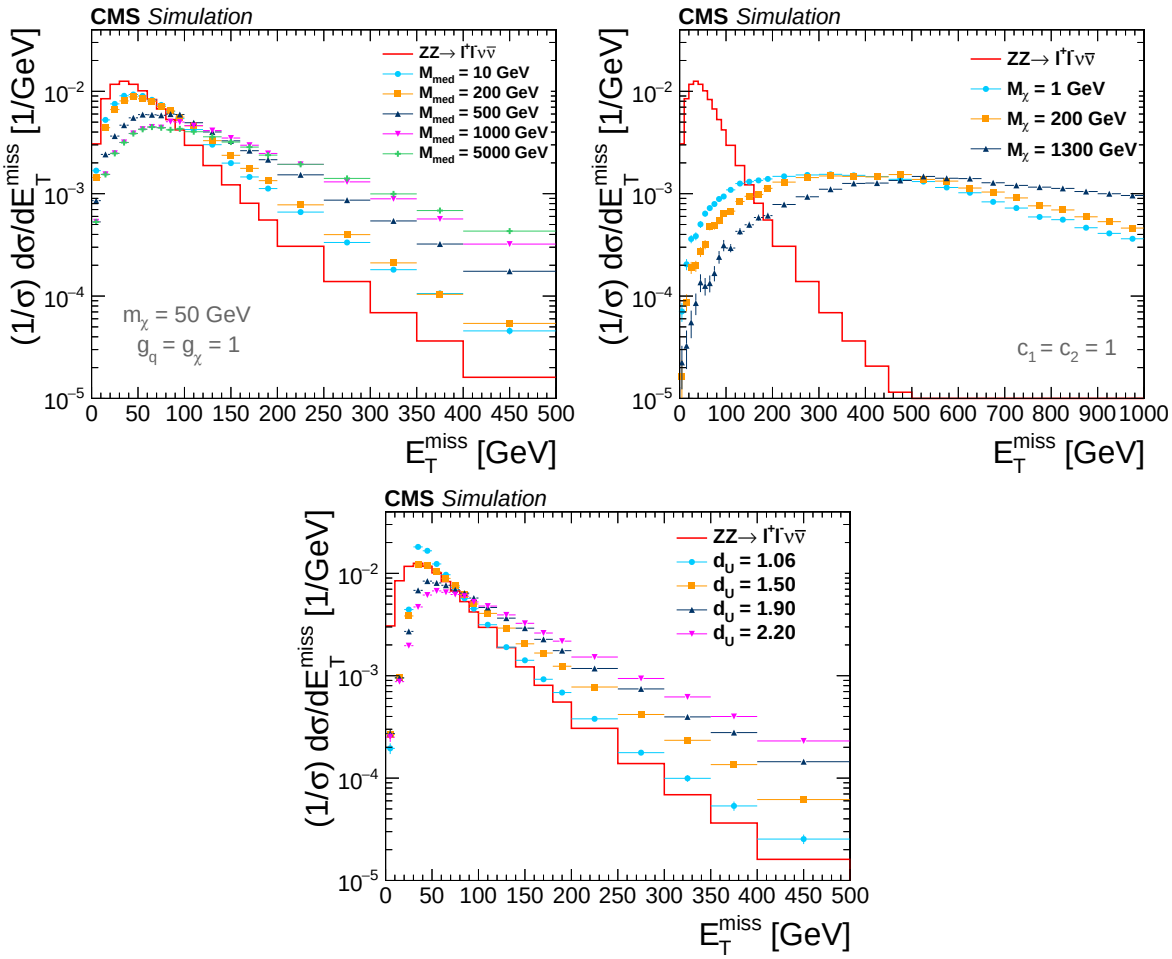

Figure 3: The distribution in $E_{\mathrm{T}}^{\mathrm{miss}}$ at the generator level, for simplified DM model with vector coupling (top left), EFT DM model (top right), and unparticle scenarios. The DM curves are shown for different values of the vector mediator mass M_{med} in the left pane and for different values of the DM mass m_χ in the right pane (note the different binning due to a much broader shape). The unparticle curves have the scalar unparticle coupling λ between unparticle and SM fields set to 1, with the scaling dimension $d_{\mathcal{U}}$ ranging from 1.06 to 2.2. The SM background $\mathrm{ZZ} \to \ell^-\ell^+\nu\overline{\nu}$ is shown as a red solid histogram.

description of the CMS detector, based on the GEANT4 package [43, 44]. Minimum bias events are superimposed on the simulated events to emulate the effect of additional pp interactions per bunch crossing (pileup). All MC samples are corrected to reproduce the pileup distribution as measured in the data. The average number of pileup interactions per proton bunch crossing is about 12 for the 2015 data sample.

4 Event reconstruction

Events are collected by requiring dilepton (ee or $\mu\mu$) triggers with thresholds of $p_T > 17$ and 12 or 8 GeV for the leading and subleading electrons or muons, respectively. Single-lepton triggers with thresholds of $p_T > 23\,(20)$ GeV for electrons (muons) are also included to recover residual trigger inefficiencies. Prior to the selection of leptons, a primary vertex must be selected as the event vertex. The vertex with largest value of $\sum p_T^2$ for the associated tracks is selected. Simulation studies show that this requirement correctly selects the event vertex in more than 99% of both signal and background events. The lepton candidate tracks are required to be compatible with the event vertex.

A particle-flow (PF) event algorithm [45, 46] reconstructs and identifies each individual particle with an optimized combination of information from the various elements of the CMS detector. The energy of photons is directly obtained from the ECAL measurement, corrected for the zero-suppression effects. The energy of electrons is determined from a combination of the electron momentum at the event vertex as determined by the tracker, the energy of the corresponding ECAL cluster, and the energy sum of all bremsstrahlung photons spatially compatible with originating from the electron track. The energy of muons is obtained from the curvature of the corresponding track. The energy of charged hadrons is determined from a combination of its momentum measured in the tracker and the matching ECAL and HCAL energy deposits, corrected for the zero-suppression effects and for the response function of the calorimeters to hadronic showers. Finally, the energy of neutral hadrons is obtained from the corresponding corrected ECAL and HCAL energy.

Electron candidates are reconstructed using an algorithm that combines information from the ECAL and the tracker [47]. To reduce the electron misidentification rate, the candidates have to satisfy additional identification criteria that are based on the shape of the electromagnetic shower in the ECAL. In addition, the electron track is required to originate from the event vertex and to match the shower cluster in the ECAL. Electron candidates with an ECAL cluster in the transition region between ECAL barrel and endcap ($1.44 < |\eta| < 1.57$) are rejected because the reconstruction of an electron candidate in this region is not optimal. Candidates that are identified as coming from photon conversions [47] in the detector material are explicitly removed.

Muon candidate reconstruction is based on two algorithms: in the first, tracks in the silicon tracker are matched with at least one muon segment in any detector plane of the muon system, and in the second algorithm a combined fit is performed to hits in both the silicon tracker and the muon system [48]. The muon candidates in this analysis are required to be reconstructed with both algorithms and to be further identified as muons by the PF algorithm. To reduce the muon misidentification rate, additional identification criteria are applied based on the number of spatial points measured in the tracker and in the muon system, the fit quality of the muon track, and its consistency with the event vertex location.

The identification of τ leptons decaying hadronically (τ_h) is performed using the "hadron-plus-strips" (HPS) algorithm. The algorithm requires a jet with an identified subset of particles with

a mass consistent with the decay products of a τ_h [49]. The decay modes of the τ_h consist of either one or three charged hadrons along with up to two neutral pions. The decay of neutral pions usually appears as "strips" in the ECAL segments which, together with the charged hadron tracks consistent with a τ_h decay, are then combined to form a τ_h candidate. The τ_h candidate is furthermore required to be isolated using a set of isolation discriminators within a radial cone size $R = \sqrt{(\Delta\eta)^2 + (\Delta\phi)^2} < 0.3$, where ϕ is the azimuthal angle. The HPS algorithm has been optimized for τ_h candidates with $p_T > 20\,\text{GeV}$.

Leptons produced in the decay of Z bosons are expected to be isolated from hadronic activity in the event. Therefore, an isolation requirement is applied based on the sum of the momenta of the PF candidates found in a cone of radius $\Delta R = 0.4$ around each lepton. The isolation sum is required to be smaller than 15% (20%) of the p_T of the electron (muon). For each electron, the mean energy deposit in the isolation cone of the electron, coming from other pp collisions in the same bunch crossing, is estimated Following the method described in Ref. [47], and subtracted from the isolation sum. For muon candidates, only charged tracks associated with the event vertex are included. The sum of the p_T for charged particles not associated with the event vertex in the cone of interest is rescaled by a factor of 0.5, corresponding to the average neutral to charged energy density ratio in jets, and subtracted from the isolation sum.

Jets are reconstructed from PF candidates by using the anti-k_t clustering algorithm [50] with a distance parameter of 0.4, as implemented in the FastJet package [51, 52]. Jets are found over the full calorimeter acceptance, $|\eta| < 5$. The jet momentum is defined as the vector sum of all particle momenta assigned to the jet, and is found in the simulation to be within 5 to 10% of the true hadron-level momentum over the whole p_T range and detector acceptance. An overall energy subtraction is applied to correct for the extra energy clustered in jets due to pileup, following the procedure described in Ref. [53]. In the subtraction, the charged-particle candidates associated with secondary vertices reconstructed in the event are also included. Other jet energy scale corrections applied are derived from simulation, and are complemented by measurements of the energy balance in dijet and γ+jets events.

5 Event selection

An initial preselection with a large yield is used to validate the background model and is followed by a final selection that is designed to give maximal sensitivity to the signal. Selected events are required to have exactly two well-identified, isolated leptons with the same flavor and opposite charge (e^+e^- or $\mu^+\mu^-$), each with $p_T > 20\,\text{GeV}$. The invariant mass of the lepton pair is required to be within $\pm 10\,\text{GeV}$ of the nominal mass of the Z boson [54]. Only electrons (muons) within the pseudorapidity range of $|\eta| < 2.5\,(2.4)$ are considered. To reduce the background from the WZ process where the W boson decays leptonically, events are removed if an additional electron or muon is reconstructed with $p_T > 10\,\text{GeV}$. The event is also removed from the final selection if an additional τ_h candidate is reconstructed with $p_T > 20\,\text{GeV}$. As a very loose preselection requirement, the dilepton transverse momentum ($p_T^{\ell\ell}$) is required to be larger than 50 GeV to reject the bulk of DY background events.

Since only a small amount of hadronic activity is expected in the final state of both DM and unparticle events, any event having two or more jets with $p_T > 30\,\text{GeV}$ is rejected. Top quark decays, which always involve the emission of b quarks, are further suppressed with the use of techniques based on soft-muon and secondary-vertex b jet tagging. Soft muons are identified using a specialised low-p_T set of identification criteria focused on track quality and the compatibility with the selected primary vertex. The rejection of events with soft muons having

$p_T > 3$ GeV reduces the background from semileptonic b decays. The b jet tagging technique employed is based on the "combined secondary vertex" algorithm [55–57]. This algorithm selects a group of tracks forming a secondary vertex within a jet and generates a likelihood discriminant to distinguish between b jets and jets originating from light quarks, gluons, or charm quarks. The applied threshold provides, on average, 80% efficiency for tagging jets originating from b quarks, and 10% probability of light-flavor jet misidentification. The b-tagged jet is required to have $p_T > 20$ GeV and to be reconstructed within the tracker acceptance volume ($|\eta| < 2.5$).

Further kinematic requirements are set in order to achieve the best possible signal extraction. At least 80 GeV of E_T^{miss} is required. The angle between the Z boson and the missing transverse energy $\Delta\phi_{\ell\ell,\vec{p}_T^{miss}}$ is required to be larger than 2.7. The balance of the event defined by $|E_T^{miss} - p_T^{\ell\ell}|/p_T^{\ell\ell}$ is required to be < 0.2. These variables effectively suppress background processes such as DY and top quark production. The final selection criteria obtained for both the electron and muon channels are summarized in Table 1.

Figure 4 shows the distributions of E_T^{miss} after preselection in the ee and $\mu\mu$ channels. Good agreement is found between the observed distributions and the background prediction, which is described in the following section.

Table 1: Summary of selections used in the analysis.

	Variable	Requirements
Preselection	p_T^{ℓ}	$>$20 GeV
	$\lvert m_{\ell\ell} - m_Z \rvert$	$<$10 GeV
	Jet counting	$\leq$1 jets with $p_T^{j} > 30$ GeV
	$p_T^{\ell\ell}$	$>$50 GeV
	3rd-lepton veto	$p_T^{e,\mu} > 10$ GeV, $p_T^{\tau} > 20$ GeV
	Top quark veto	veto on b jets and soft muon
Selection	$\Delta\phi_{\ell\ell,\vec{p}_T^{miss}}$	> 2.7 rad
	$\lvert E_T^{miss} - p_T^{\ell\ell} \rvert / p_T^{\ell\ell}$	< 0.2
	E_T^{miss}	$>$80 GeV

6 Background estimation

The ZZ and WZ backgrounds are modeled using MC simulation, and normalized to their respective NLO cross sections. Other backgrounds, including $t\bar{t}$, tW, WW, $Z \to \tau\tau$, single top quark production, and DY, are estimated from data for the final selection.

The simulation of the ZZ process includes the $q\bar{q}$- and gg-induced production modes. We apply $\Delta\phi(Z,Z)$-dependent K-factors to correct the ZZ differential cross section from the NLO to the next-to-next-to-leading order (NNLO) in QCD. We apply NLO electroweak (EW) K-factors as a function of the p_T of the trailing boson, following the calculations in Refs. [58–60]. Electroweak corrections to WZ are also available, but considered small and not applied, according to Ref. [60].

The background processes that do not involve Z boson production are referred to as nonresonant backgrounds. Such backgrounds arise mainly from leptonic W boson decays in $t\bar{t}$, tW, and WW events. There are also small contributions from s- and t-channel single top quark events, W+jets events, and $Z \to \tau\tau$ events in which τ leptons produce electrons or muons and E_T^{miss}. We estimate these nonresonant backgrounds using a data control sample, consisting of

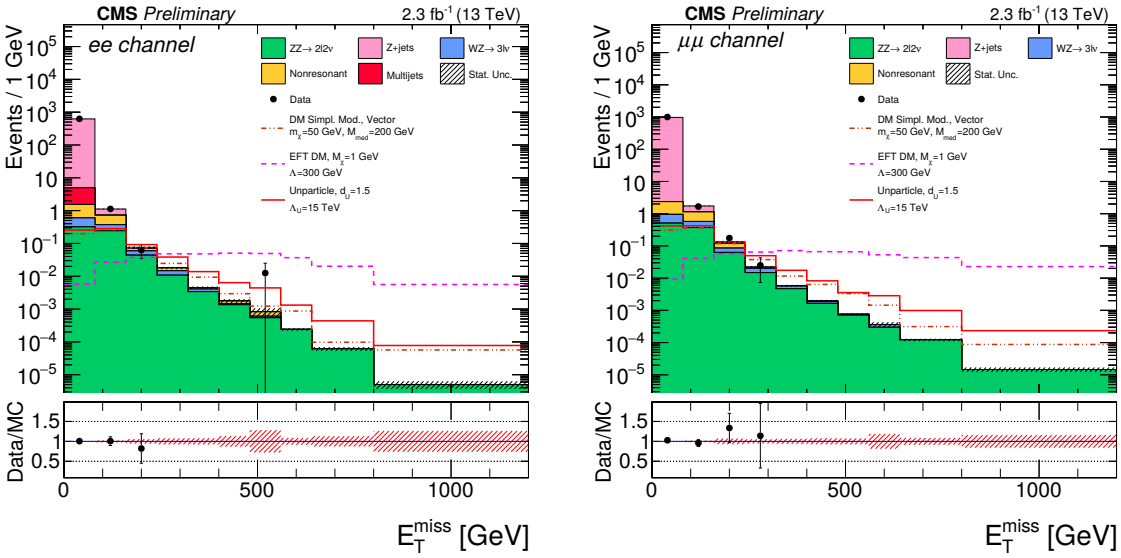

Figure 4: The distribution of $E_{\mathrm{T}}^{\mathrm{miss}}$ after preselection for the $\mathrm{Z} \to \mathrm{e}^{+}\mathrm{e}^{-}$ (left) and $\mathrm{Z} \to \mu^{+}\mu^{-}$ (right) channels. Expected signal distributions are shown for the simplified model of DM production with vector couplings, the EFT scenario of DM production, and unparticles. The shown SM expectation is based on simulation only. The total statistical uncertainty in the overall background prediction is shown as a hatched region. Overflow events are included in the rightmost bins. In the bottom panels, the ratio between data and predicted background is shown.

events with an opposite-charge different-flavor dilepton pair ($\mathrm{e}^{\pm}\mu^{\mp}$) that otherwise pass the full selection. As the decay rates for $\mathrm{Z} \to \mathrm{e}^{+}\mathrm{e}^{-}$ and $\mathrm{Z} \to \mu^{+}\mu^{-}$ are equal, by equating the ratio of observed dilepton counts to the square of the ratio of efficiencies, the backgrounds in the ee and $\mu\mu$ channels can be estimated:

$$N_{\mathrm{bkg,ee}}^{\mathrm{est}} = N_{\mathrm{e}\mu}^{\mathrm{data,\,corr}}\, k_{\mathrm{ee}}, \qquad k_{\mathrm{ee}} = \frac{1}{2}\sqrt{\frac{N_{\mathrm{ee}}^{\mathrm{data}}}{N_{\mu\mu}^{\mathrm{data}}}},$$

$$N_{\mathrm{bkg},\mu\mu}^{\mathrm{est}} = N_{\mathrm{e}\mu}^{\mathrm{data,\,corr}}\, k_{\mu\mu}, \qquad k_{\mu\mu} = \frac{1}{2}\sqrt{\frac{N_{\mu\mu}^{\mathrm{data}}}{N_{\mathrm{ee}}^{\mathrm{data}}}},$$

in which the coefficient of 1/2 in the correction factors k_{ee} and $k_{\mu\mu}$ comes from the dilepton decay ratios for ee, $\mu\mu$, and eμ in these nonresonant backgrounds, and $N_{\mathrm{ee}}^{\mathrm{data}}$ and $N_{\mu\mu}^{\mathrm{data}}$ are the numbers of selected ee and $\mu\mu$ events from data with masses in the Z boson mass window. The ratio $\sqrt{N_{\mathrm{ee}}^{\mathrm{data}}/N_{\mu\mu}^{\mathrm{data}}}$ and the reciprocal quantity take into account the difference between the electron and muon selection efficiencies. The term $N_{\mathrm{e}\mu}^{\mathrm{data,\,corr}}$ is the number of eμ events observed in data corrected by subtracting ZZ, WZ, and DY background contributions estimated using MC simulation. The kinematic distributions of the estimated nonresonant backgrounds are obtained from simulation with the overall normalization determined by the method described above. The validity of this procedure for predicting nonresonant backgrounds is checked with simulated events containing $\mathrm{t\bar{t}}$, tW, WW, W+jets, and $\mathrm{Z} \to \tau\tau$ processes. We assign a systematic uncertainty of 26% for this background estimation in both the electron and muon channels for $E_{\mathrm{T}}^{\mathrm{miss}} > 80\,\mathrm{GeV}$, based on closure tests that compare the predictions obtained from the control sample with those from the simulated events.

The DY process is dominant in the region of low $E_{\mathrm{T}}^{\mathrm{miss}}$. This process does not produce undetectable particles, and therefore the measured $E_{\mathrm{T}}^{\mathrm{miss}}$ arises from limited detector acceptance and mismeasurement. The estimation of this background uses simulated DY events, which

are normalized to data with scale factors obtained by measuring the number of DY events in a background-dominated control region, after subtracting other processes. These scale factors are of order 1.0–1.2. The control region is defined by applying the full selection except inverting the $E_{\mathrm{T}}^{\mathrm{miss}}$ requirement. The reliability of this approach in the high-$E_{\mathrm{T}}^{\mathrm{miss}}$ regime has been studied by considering variables sensitive to $E_{\mathrm{T}}^{\mathrm{miss}}$ mismeasurement, such as the angular separation between the $E_{\mathrm{T}}^{\mathrm{miss}}$ direction and any jet. A normalization uncertainty of 100%, which accomodates any differences observed in these control regions, is assigned for the DY background estimate. The assigned uncertainty has little impact on the overall signal sensitivity because of the small overall contribution from the DY background prediction.

7 Efficiencies and systematic uncertainties

The efficiencies for selecting, reconstructing, and identifying isolated leptons are determined from simulation, and then corrected with scale factors determined from applying a "tag-and-probe" technique [61] to $\mathrm{Z} \to \ell^+\ell^-$ events. The trigger efficiencies for the electron and muon channels are found to be above 90%, varying as a function of p_{T} and $|\eta|$ of the lepton. The identification efficiency for electrons (muons), when applying the selection criteria described in Section 4, is found to be about 80–86% (95%) depending on the p_{T} and η of the corresponding lepton. The corresponding data-to-MC scale factors are typically in the range 0.96–1.00 (0.96–0.98) for the electron (muon) channel, depending on the p_{T} and $|\eta|$ of the lepton candidate. The lepton momentum scale uncertainty is computed by varying the momentum of the leptons by their uncertainties. We assume this uncertainty for the muons to be 1% and the uncertainty for the electrons to be 2% for the barrel and 5% for the endcaps. For both channels, the overall uncertainty in selecting and reconstructing leptons in an event is about 3%.

The systematic uncertainties include normalization uncertainties that affect the overall size of contributions, and shape uncertainties that alter the shapes of the distributions used in extracting the signal limits. The systematic uncertainties are summarized in Table 2. The impact of each group of uncertainties on a potential signal strength observation is also reported. To calculate it, a maximum likelihood fit of the combined background and signal model to the expected distribution for unity signal strength. The fit is repeated with each individual nuisance parameter varied up and down within its uncertainty. The impact of the uncertainty is then defined as the relative change induced in the expected best fit signal strength by the variation of the respective parameter. In the table, the reference signal is the simplified model DM scenario with a vector mediator of mass 200 GeV and a DM particle mass of 50 GeV.

The normalization uncertainties in the background estimates from data are described in Section 6. The PDF and α_S uncertainties (referred to as PDF+α_S in the following) for signal and background processes are estimated from the standard deviation of weights from the replicas provided in the NNPDF3.0 parton distribution set [42]. For the signal processes, only the influence of the theory-related uncertainties on the acceptance is considered. The influence on the normalisation of the signal processes is given separately for the simplified model DM scenario. For the unparticle and EFT benchmark scenarios, the normalisation uncertainty is not taken into account. This choice reflects the schematic nature of the EFT signal models. The efficiencies for signal, ZZ, and WZ processes are estimated using simulation, and the uncertainties in the corresponding yields are derived from variations of the renormalization and factorization scales, α_S, and choice of PDFs. The factorization and renormalization scale uncertainties are assessed by varying the original scales of the process by factors of 0.5 and 2, and amount to 2–3% for ZZ and WZ processes. The effect of variations in α_S and choice of PDFs is 2% for the ZZ and WZ backgrounds. A 3% normalisation uncertainty is assigned to the WZ background

Table 2: Summary of systematic uncertainties. Each background uncertainty represents the variation of the relative yields of the particular background components. The signal uncertainties represent the relative variations in the signal acceptance, and ranges quoted cover both signals of DM and unparticles with different DM masses or scaling dimensions. For shape uncertainties, the numbers correspond to the overall effect of the shape variation on the yield or acceptance. The symbol "—" indicates that the systematic uncertainty is not applicable. The impact of the each group of systematic uncertainties is calculated by performing a maximum likelihood fit to obtain the signal strength with each parameter separately varied up and down within its uncertainty. The number given in the impact column is the relative change of the-expected best fit signal strength that is introduced by the variation for a the simplified model signal scenario with a vector mediator of mass 200 GeV and DM of mass 50 GeV.

Source of uncertainty	Background uncertainty (%)	Signal uncertainty (%)	Impact (%)
Integrated luminosity	2.7	2.7	5
Lepton trigger & identification efficiency	3-4	3-4	2-4
Lepton momentum scale, resolution	1-7	< 1	1-2
Jet energy scale, resolution	0.1-4	< 1	2
b jet tagging efficiency	< 1	< 1	< 1
Pileup	1-2	0.5-1	2
PDF, α_S	2-3	< 1	< 1
Factorization, renormalization scales (signal)	—	1-2	< 1
Factorization, renormalization scales (VV)	3-4	—	3
Factorization, renormalization scales (VVV)	12	—	< 1
Electroweak correction for $q\bar{q} \to ZZ$	5	—	4
Electroweak uncertainty for WZ	3	—	< 1
DY normalization	100	—	5
$t\bar{t}$, tW, WW normalization	26	—	2-4
MC statistics (signal)	—	1.5-10	< 1
MC statistics (ZZ, WZ, VVV)	1-20	—	< 1
MC statistics (DY)	30-50	—	< 1
MC statistics ($t\bar{t}$, tW, WW)	8-10	—	< 1

to account for higher-order EW corrections. The uncertainty assigned for the integrated luminosity measurement is 2.7% [62].

The contributions to the shape uncertainties come from the lepton momentum scale, the jet energy scale and resolution, the b tagging efficiency, and the pileup modeling. Each corresponding uncertainty is calculated by varying the respective variable of interest within its own uncertainties, and propagating the variations to the variable E_T^{miss} using the final selection. In the case of the lepton momentum scale, the uncertainty is computed by varying the momentum of the leptons by their uncertainties. The uncertainty in the lepton momentum scale is evaluated to be less than 1% (1–7%) for signal (background).

The uncertainties in the calibration of the jet energy scale and resolution directly affect the assignments of jets to jet categories, the E_T^{miss} computation, and all the selections related to jets. The effect of the jet energy scale uncertainty is estimated by varying the energy scale by $\pm 1\sigma$. A similar strategy is used to evaluate the systematic uncertainty related to the jet energy resolution. The effect of the shifts is propagated to E_T^{miss}. The uncertainties in the final yields are found to be less than 1% (up to 4%) for signal (background). Since the b tagging efficiencies measured in data are somewhat different from those predicted by the simulation, an event-by-

event reweighting using data-to-simulation scale factors is applied to simulated events. The uncertainty associated with this procedure is obtained by varying the event-by-event weight by $\pm 1\sigma$. The total uncertainty in the final yields is less than 1% for both signal and background. All simulated events are reweighted to reproduce the pileup conditions observed in data. To compute the uncertainty related to pileup modeling, we shift the mean of the distribution in simulation by 5% [63]. The variation of the final yields induced by this procedure is 0.5–1% (1–2%) for signal (background). For the processes estimated from simulation, the sizes of the MC samples limit the precision of the modeling, and the corresponding statistical uncertainty is incorporated into the shape uncertainty. A similar treatment is applied to the backgrounds estimated from control samples in data based on the statistical uncertainties in the corresponding control samples.

8 Results

For both the electron and the muon channels, a shape-based analysis is employed. The expected numbers of background and signal events scaled by a signal strength modifier are combined in a binned likelihood for each bin of the $E_{\mathrm{T}}^{\mathrm{miss}}$ distribution. The signal strength modifier, defined as the signal cross section divided by the cross section suggested by theory, determines the strength of the signal process. The numbers of observed and expected events are shown in Table 3, including the expectation for a selected mass point for each type of signal. Figure 5 shows the $E_{\mathrm{T}}^{\mathrm{miss}}$ distributions after the final selection. The observed distributions agree with the SM background predictions and no excess of events is observed.

Table 3: Signal predictions and background estimates for the final selection with $E_{\mathrm{T}}^{\mathrm{miss}} > 80$ GeV. The DM signal yields from the simplified model are given for mass $m_\chi = 50$ GeV and mediator masses $M_{\mathrm{med}} = 200$ GeV for the vector and axial-vector coupling scenarios. For the EFT benchmark model with DM pair coupling to gauge bosons, the signal yields are given for $m_\chi = 1$ GeV, cutoff scale $\Lambda = 300$ GeV, and the couplings $c_1 = c_2 = 1$. The corresponding statistical and systematic uncertainties are shown, in that order.

Process	$\mathrm{e^+e^-}$	$\mu^+\mu^-$
Simplified DM model, vector coupling $m_\chi = 50$ GeV, $M_{\mathrm{med}} = 200$ GeV	$15.8 \pm 0.4 \pm 1.0$	$25.5 \pm 0.5 \pm 1.8$
Simplified DM model, axial-vector coupling $m_\chi = 50$ GeV, $M_{\mathrm{med}} = 200$ GeV	$12.9 \pm 0.3 \pm 0.9$	$19.2 \pm 0.4 \pm 1.3$
EFT DM model $m_\chi = 1$ GeV, $\Lambda = 300$ GeV	$25.4 \pm 0.4 \pm 2.7$	$47.7 \pm 0.5 \pm 5.9$
$\mathrm{Z}/\gamma^* \to \ell^+\ell^-$	$4.9 \pm 0.6 \pm 4.9$	$5.3 \pm 0.7 \pm 5.3$
$\mathrm{WZ} \to 3\ell\nu$	$4.6 \pm 0.2 \pm 0.4$	$7.0 \pm 0.2 \pm 0.6$
$\mathrm{ZZ} \to 2\ell 2\nu$	$12.4 \pm 0.1 \pm 1.0$	$18.7 \pm 0.1 \pm 1.5$
$\mathrm{t\bar{t}/tW/WW/Z} \to \tau\tau$	$7.0 \pm 1.0 \pm 1.9$	$14.0 \pm 2.1 \pm 3.8$
VVV, $\mathrm{ZZ} \to 2\ell 2q, 4\ell$	< 0.1	< 0.1
Total background	$28.9 \pm 1.2 \pm 5.4$	$45.0 \pm 2.2 \pm 6.8$
Data	22	44

Upper limits on the contribution of events from new physics are computed by using the modified frequentist approach $\mathrm{CL_s}$ [64, 65] based on asymptotic formulas [66, 67].

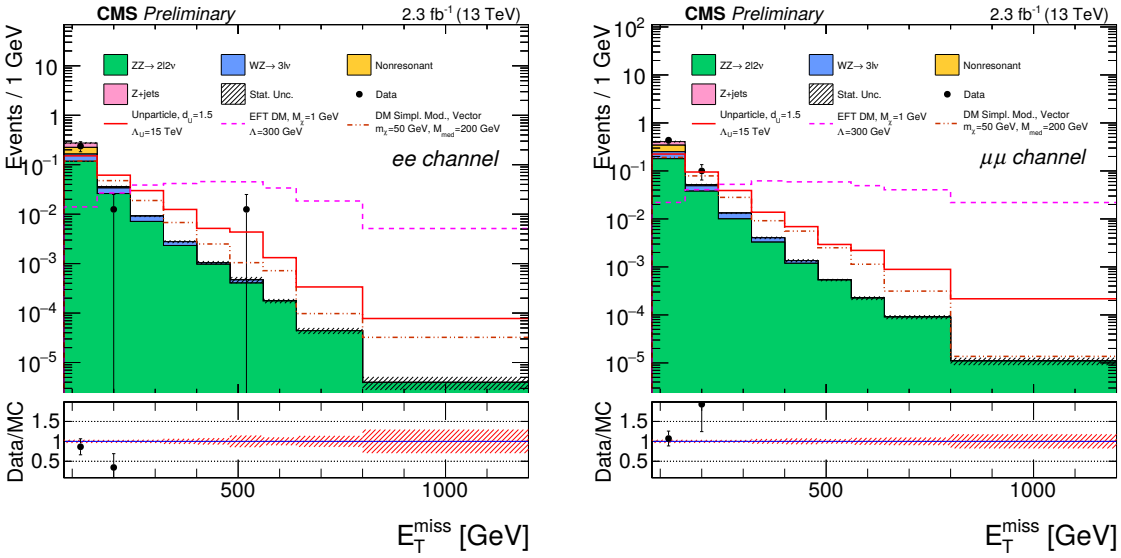

Figure 5: Distributions of the $E_{\mathrm{T}}^{\mathrm{miss}}$ for the final selection in the $\mathrm{e^+e^-}$ (left) and $\mu^+\mu^-$ (right) channels. Expected signal distributions are shown for the simplified model of DM production with vector couplings, the EFT scenario of DM production, and unparticles. The statistical uncertainty in the overall background is shown as a hatched region. Overflow events are included in the rightmost bins. In the bottom panels, the ratio between data and predicted background is shown.

8.1 The DM interpretation

The results are interpreted in the context of a simplified model of DM production. Figure 6 shows 95% confidence level (CL) expected and observed limits on the signal strength $\sigma^{\mathrm{obs}}/\sigma^{\mathrm{th}}$, in the case of vector and axial-vector mediators, and for two possible values of the quark-mediator coupling constant, $g_{\mathrm{q}} = 0.25$ or 1. The DM-nucleon scattering cross sections in both spin-independent (vector) and spin-dependent (axial-vector) cases are shown in Fig. 7, assuming $g_{\mathrm{q}} = 0.25$. In all cases, the DM-mediator coupling g_χ is set to one.

Figure 8 shows 95% CL expected limits on the cutoff scale Λ of the EFT benchmark model with DM pair coupling to gauge bosons, the limits are plotted as a function of DM mass. The 95% CL expected limits on the cutoff scale Λ and signal strength $\sigma^{\mathrm{obs}}/\sigma^{\mathrm{th}}$ as a function of coupling c_1 and DM mass m_χ are shown in Fig. 9. At $c_1 \approx c_2$, the interaction is dominated by the $ZZ\chi\chi$-vertex. With increasing c_1, the $\gamma Z\chi\chi$-vertex begins to contribute, yielding an improvement in the sensitivity.

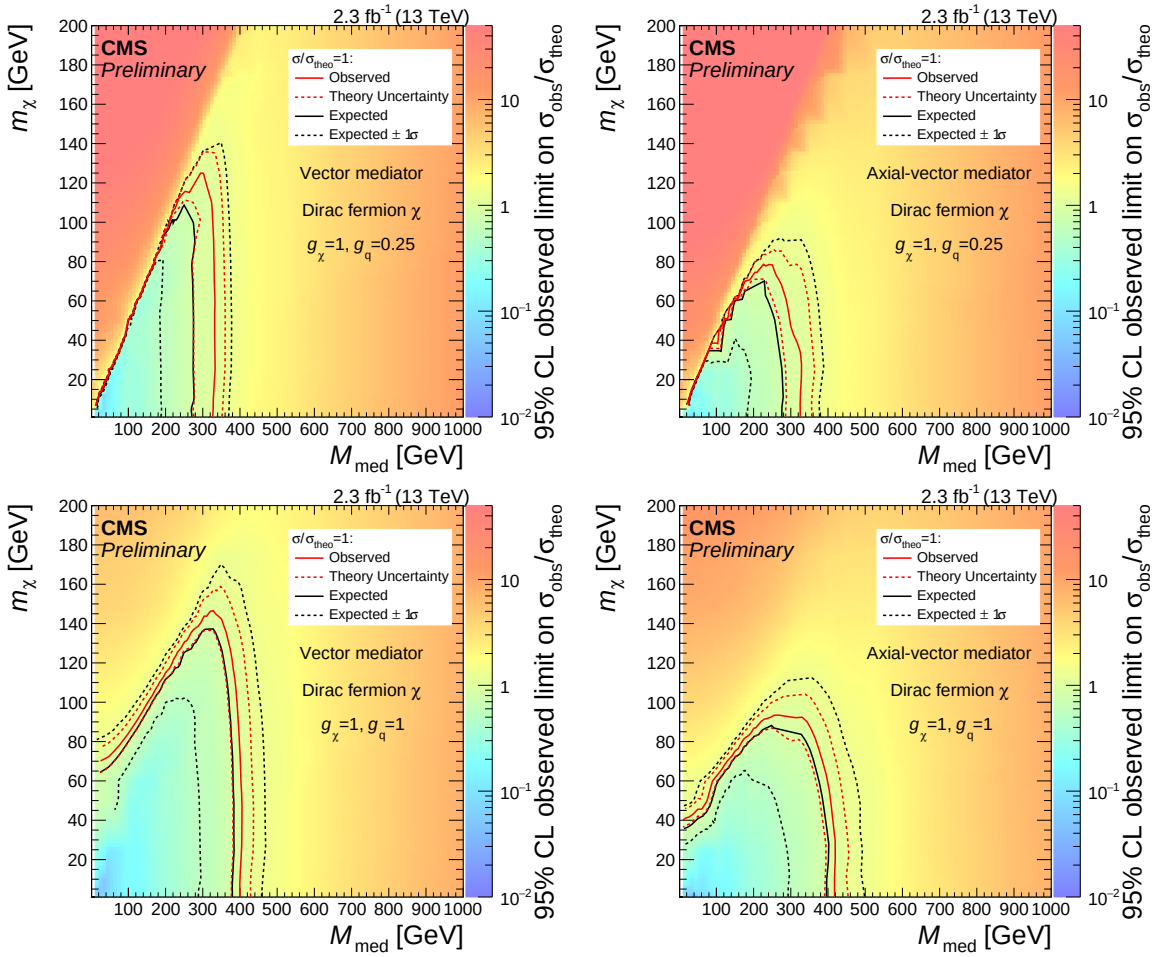

Figure 6: The 95% CL observed limits on the signal strength $\sigma_{\text{obs}}/\sigma_{\text{theo}}$ in both vector (left) and axial-vector (right) mediator scenarios, for mediator-quark coupling constant values $g_{\text{q}} = 0.25$ (upper) and 1 (lower). In all cases, the DM-mediator coupling g_χ is set to one. The expected exclusion curves for unity signal strength are shown as a reference. The red dashed lines show the influence of theory-related signal normalization uncertainties on the observed limits, which are estimated to be 15%.

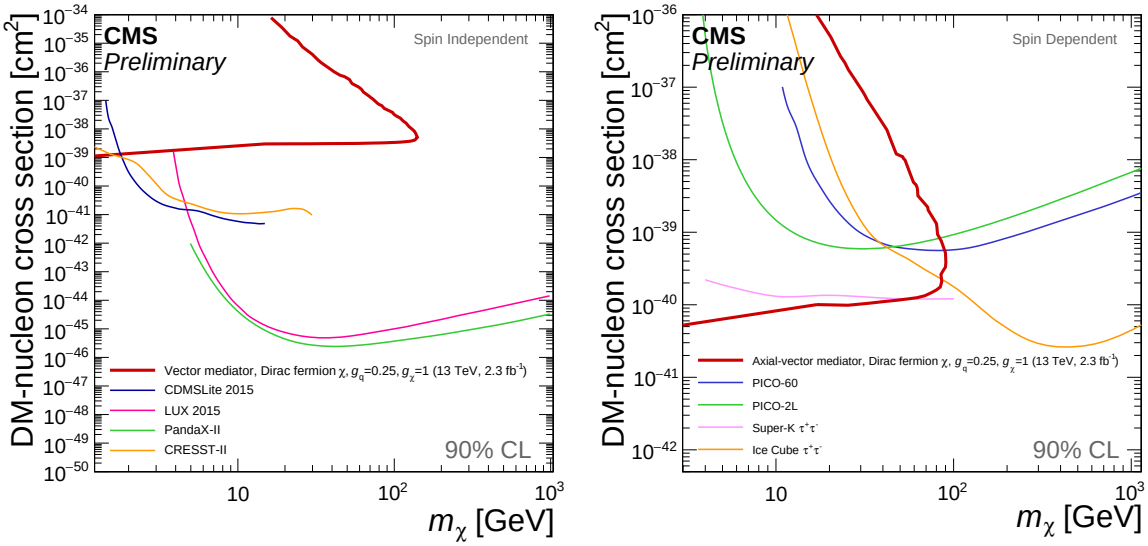

Figure 7: Observed 90% CL limits on the DM-nucleon scattering cross sections in both spin-independent (left) and spin-dependent (right) cases, assuming a mediator-quark coupling constant $g_q = 0.25$ and mediator-DM coupling constant $g_\chi = 1$. Limits from the LUX [68], CDMSLite [69], PandaX-II [70], and CRESST-II [71] experiments are shown for the spin-independent case. Limits from the Super-Kamiokande [72], PICO-2L [73], PICO-60 [74], and IceCube [75] experiments are shown for the spin-dependent case.

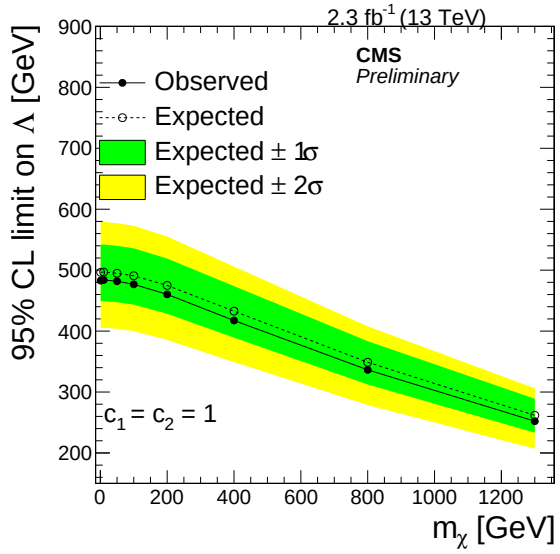

Figure 8: The 95% CL expected and observed limits on the cutoff scale Λ as a function of DM mass m_χ.

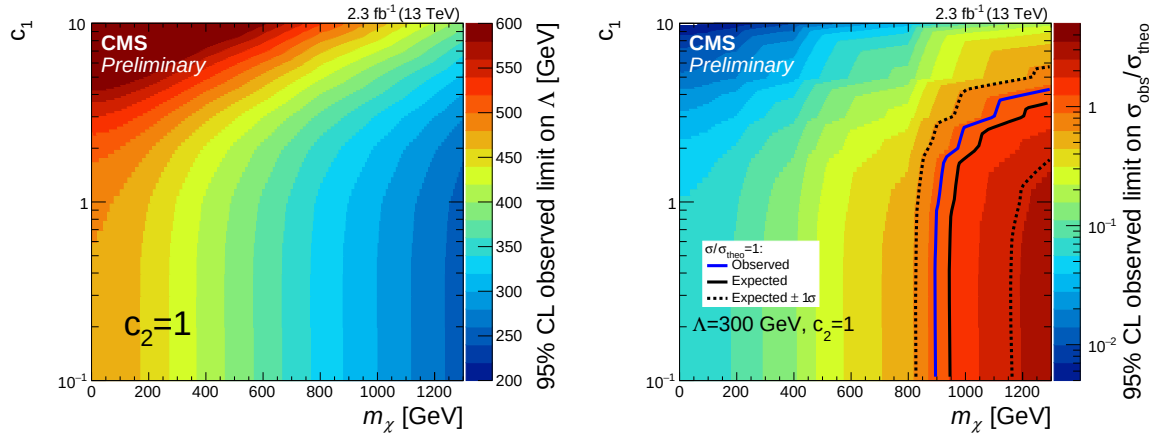

Figure 9: The 95% CL observed limits on the cutoff scale Λ (left) and signal strength $\sigma^{\text{obs}}/\sigma^{\text{th}}$ (right) as a function of coupling c_1 and DM mass m_χ. The expected exclusion curves for unity signal strength are shown as a reference.

8.2 Unparticle interpretation

In the scenario of the unparticle model, the 95% CL lower limits the effective cutoff scale $\Lambda_{\mathcal{U}}$ with a fixed coupling $\lambda = 1$, are shown in Fig. 10. It compares the result with the limits obtained from previous CMS searches in the monojet [3] and mono-Z [17] channels as well as to a reinterpretation of LEP searches [76].

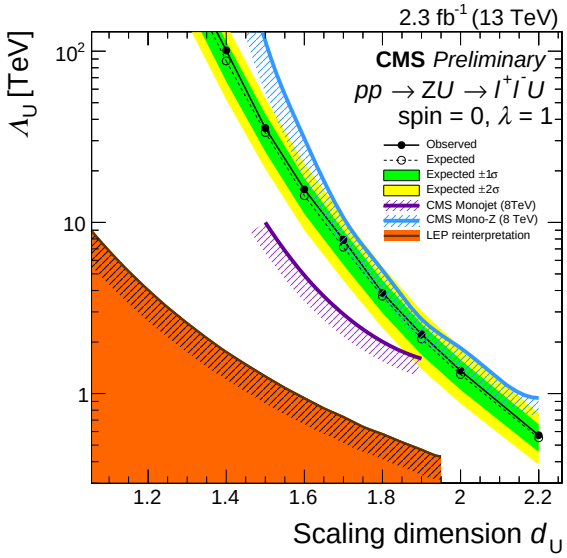

Figure 10: The 95% CL lower limits on unparticle effective cutoff scale $\Lambda_{\mathcal{U}}$ with a fixed coupling $\lambda = 1$. The results from CMS monojet [3] and mono-Z [17] searches, as well as a reinterpretation of LEP searches [76] are shown for comparison.

8.3 Model-independent limits

As an alternative to the interpretation of the results in specific models, a single-bin analysis is applied to obtain model-independent expected and observed 95% CL upper limits on the visible cross section $\sigma_{\text{vis}}^{\text{BSM}}$ for beyond the standard model (BSM) physics processes. The limits as a function of $E_{\text{T}}^{\text{miss}}$ thresholds are shown in Fig. 11. Table 4 shows the total SM background predictions for the numbers of events passing the selection requirements, for different $E_{\text{T}}^{\text{miss}}$ thresholds, compared with the observed numbers of events. The 95% CL expected and observed upper limits for the contribution of events from BSM sources are also shown. Since the efficiency of reconstructing potential signal events depends on the characteristics of the signal, the model-independent limits are not corrected for the efficiency. For the models considered in this analysis, typical efficiencies range 50–70% (simplified DM model), 60–70% (EFT DM model), and 55–60% (unparticle model). The efficiencies are calculated as the ratio of the number of simulated events passing the final selection and the number of simulated events passing the selection criteria at the generator level.

9 Summary

A search is performed with the final state of a Z boson plus missing transverse energy on a dataset corresponding to an integrated luminosity of 2.3 fb^{-1} of pp collisions at a center-of-mass energy of 13 TeV. The observed data are consistent with the expected SM backgrounds. The results are analyzed to obtain limits in three different scenarios of physics beyond the SM. In a simplified model of DM production via a vector or axial vector mediator, 95% CL limits

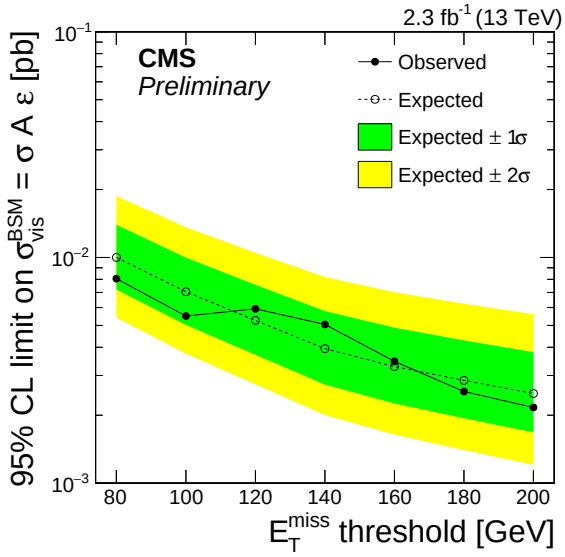

Figure 11: The model-independent upper limits at 95% CL on the visible cross section ($\sigma\, A\, \epsilon$) for BSM production of events, as a function of $E_{\mathrm{T}}^{\mathrm{miss}}$ threshold.

Table 4: Total SM background predictions for the numbers of events passing the selection requirements, for different $E_{\mathrm{T}}^{\mathrm{miss}}$ thresholds, compared with the observed numbers of events. The listed uncertainties include both statistical and systematic components. The 95% CL observed and expected upper limits for the contribution of events from BSM sources are also shown. The $\pm 1\sigma$ and $\pm 2\sigma$ excursions from expected limits are also given.

$E_{\mathrm{T}}^{\mathrm{miss}}$ threshold (GeV)	80	100	120	140	160	180	200
Total SM	73.9	43.0	24.0	14.1	9.5	6.8	4.9
Total uncertainty	$\pm$ 9.2	$\pm$ 5.2	$\pm$ 2.9	$\pm$ 1.3	$\pm$ 0.9	$\pm$ 0.7	$\pm$ 0.5
Data	66	37	26	17	10	6	4
Obs. upper limit	18.5	12.7	13.6	11.6	8.0	5.9	5.0
Exp. upper limit +2σ	43.0	31.3	24.1	18.8	16.1	14.3	12.9
Exp. upper limit +1σ	32.1	23.0	17.4	13.3	11.2	9.9	8.8
Exp. upper limit	23.0	16.2	12.1	9.1	7.6	6.6	5.7
Exp. upper limit -1σ	16.6	11.6	8.5	6.3	5.2	4.5	3.9
Exp. upper limit -2σ	12.5	8.6	6.3	4.6	3.8	3.2	2.8

are obtained on the masses of the DM particles and the mediator. Limits on the DM-nucleon scattering cross section are set at 90% CL in spin-dependent and spin-independent coupling scenarios. In an effective field theory model, limits are set on the DM coupling parameters to $U(1)$ and $SU(2)$ gauge fields and on the scale of new physics. For an unparticle model, 95% CL limits are obtained on the effective cutoff scale as a function of the scaling dimension. In addition, model-independent limits on the contribution to the visible Z +$E_{\mathrm{T}}^{\mathrm{miss}}$ cross section from non-SM sources are presented as a function of the minimum requirement on $E_{\mathrm{T}}^{\mathrm{miss}}$.

References

[1] P. Cushman et al., "Snowmass CF1 Summary: WIMP Dark Matter Direct Detection", (2013). arXiv:1310.8327.

[2] J. Buckley et al., "Indirect Dark Matter Detection CF2 Working Group Summary", (2013). arXiv:1310.7040.

[3] CMS Collaboration, "Search for dark matter, extra dimensions, and unparticles in monojet events in proton-proton collisions at $\sqrt{s}$ = 8 TeV", *Eur. Phys. J. C* **75** (2015) 235, doi:10.1140/epjc/s10052-015-3451-4, arXiv:1408.3583.

[4] CMS Collaboration, "Search for dark matter with jets and missing transverse energy at 13 TeV", CMS Physics Analysis Summary CMS-PAS-EXO-15-003, CERN, Geneva, 2016.

[5] ATLAS Collaboration, "Search for new phenomena in final states with an energetic jet and large missing transverse momentum in pp collisions at $\sqrt{s} = 8$ TeV with the ATLAS detector", *Eur. Phys. J. C* **75** (2015) 299, doi:10.1140/epjc/s10052-015-3517-3, arXiv:1502.01518.

[6] CMS Collaboration, "Search for new phenomena in monophoton final states in proton-proton collisions at $\sqrt{s} = 8$ TeV", *Phys. Lett.* **B755** (2016) 102–124, doi:10.1016/j.physletb.2016.01.057, arXiv:1410.8812.

[7] ATLAS Collaboration, "Search for new phenomena in events with a photon and missing transverse momentum in pp collisions at $\sqrt{s} = 8$ TeV with the ATLAS detector", *Phys. Rev. D* **91** (2015) 012008, doi:10.1103/PhysRevD.91.012008, arXiv:1411.1559.

[8] CMS Collaboration, "Search for physics beyond the standard model in final states with a lepton and missing transverse energy in proton-proton collisions at $\sqrt{s}$ = 8 TeV", *Phys. Rev. D* **91** (2015) 092005, doi:10.1103/PhysRevD.91.092005, arXiv:1408.2745.

[9] ATLAS Collaboration, "Search for dark matter in events with heavy quarks and missing transverse momentum in pp collisions with the ATLAS detector", *Eur. Phys. J. C* **75** (2015) 92, doi:10.1140/epjc/s10052-015-3306-z, arXiv:1410.4031.

[10] ATLAS Collaboration, "Search for dark matter in events with a hadronically decaying W or Z boson and missing transverse momentum in pp collisions at $\sqrt{s}$ = 8 TeV with the ATLAS detector", *Phys. Rev. Lett.* **112** (2014) 041802, doi:10.1103/PhysRevLett.112.041802, arXiv:1309.4017.

[11] ATLAS Collaboration, "Search for new particles in events with one lepton and missing transverse momentum in pp collisions at $\sqrt{s}$ = 8 TeV with the ATLAS detector", *JHEP* **09** (2014) 037, doi:10.1007/JHEP09(2014)037, arXiv:1407.7494.

[12] ATLAS Collaboration, "Search for invisible particles produced in association with single-top-quarks in proton-proton collisions at $\sqrt{s}$ = 8 TeV with the ATLAS detector", *Eur. Phys. J. C* **75** (2015) 79, doi:10.1140/epjc/s10052-014-3233-4, arXiv:1410.5404.

[13] ATLAS Collaboration, "Search for Dark Matter in Events with Missing Transverse Momentum and a Higgs Boson Decaying to Two Photons in pp Collisions at $\sqrt{s} = 8$ TeV with the ATLAS Detector", *Phys. Rev. Lett.* **115** (2015), no. 13, 131801, doi:10.1103/PhysRevLett.115.131801, arXiv:1506.01081.

[14] CMS Collaboration, "Search for Monotop Signatures in Proton-Proton Collisions at $\sqrt{s} = 8$ TeV", *Phys. Rev. Lett.* **114** (2015) 101801, doi:10.1103/PhysRevLett.114.101801, arXiv:1410.1149.

[15] CMS Collaboration, "Search for the production of dark matter in association with top-quark pairs in the single-lepton final state in proton-proton collisions at $\sqrt{s} = 8$ TeV", *JHEP* **06** (2015) 121, doi:10.1007/JHEP06(2015)121, arXiv:1504.03198.

[16] ATLAS Collaboration, "Search for dark matter in events with a Z boson and missing transverse momentum in pp collisions at $\sqrt{s} = 8$ TeV with the ATLAS detector", *Phys. Rev. D* **90** (2014) 012004, doi:10.1103/PhysRevD.90.012004, arXiv:1404.0051.

[17] CMS Collaboration, "Search for dark matter and unparticles produced in association with a Z boson in proton-proton collisions at $\sqrt{s} = 8$ TeV", *Phys. Rev.* **D93** (2016) 052011, doi:10.1103/PhysRevD.93.052011, arXiv:1511.09375.

[18] D. Abercrombie et al., "Dark Matter Benchmark Models for Early LHC Run-2 Searches: Report of the ATLAS/CMS Dark Matter Forum", (2015). arXiv:1507.00966.

[19] H. Georgi, "Unparticle physics", *Phys. Rev. Lett.* **98** (2007) 221601, doi:10.1103/PhysRevLett.98.221601, arXiv:hep-ph/0703260.

[20] H. Georgi, "Another odd thing about unparticle physics", *Phys. Lett. B* **650** (2007) 275, doi:10.1016/j.physletb.2007.05.037, arXiv:0704.2457.

[21] K. Cheung, W.-Y. Keung, and T.-C. Yuan, "Collider signals of unparticle physics", *Phys. Rev. Lett.* **99** (2007) 051803, doi:10.1103/PhysRevLett.99.051803, arXiv:0704.2588.

[22] K. Cheung, W.-Y. Keung, and T.-C. Yuan, "Collider Phenomenology of Unparticle Physics", *Phys. Rev. D* **76** (2007) 055003, doi:10.1103/PhysRevD.76.055003, arXiv:0706.3155.

[23] Z. Kang, "Upgrading sterile neutrino dark matter to FI*m*P using scale invariance", *Eur. Phys. J.* **C75** (2015) 471, doi:10.1140/epjc/s10052-015-3702-4, arXiv:1411.2773.

[24] M. Rinaldi, G. Cognola, L. Vanzo, and S. Zerbini, "Inflation in scale-invariant theories of gravity", *Phys. Rev. D* **91** (2015) 123527, doi:10.1103/PhysRevD.91.123527, arXiv:1410.0631.

[25] H. Cheng, "The Possible Existence of Weyl's Vector Meson", *Phys. Rev. Lett.* **61** (1988) 2182, doi:10.1103/PhysRevLett.61.2182.

[26] T. Banks and A. Zaks, "On the phase structure of vector-like gauge theories with massless fermions", *Nucl. Phys. B* **196** (1982) 189, doi:10.1016/0550-3213(82)90035-9.

[27] CMS Collaboration, "The CMS experiment at the CERN LHC", *JINST* **3** (2008) S08004, doi:10.1088/1748-0221/3/08/S08004.

[28] J. Alwall et al., "The automated computation of tree-level and next-to-leading order differential cross sections, and their matching to parton shower simulations", *JHEP* **07** (2014) 079, doi:10.1007/JHEP07(2014)079, arXiv:1405.0301.

[29] T. Sjöstrand, S. Mrenna, and P. Z. Skands, "A brief introduction to PYTHIA 8.1", *Comput. Phys. Commun.* **178** (2008) 852, doi:10.1016/j.cpc.2008.01.036, arXiv:0710.3820.

[30] CMS Collaboration, "Event generator tunes obtained from underlying event and multiparton scattering measurements", *Eur. Phys. J.* **C76** (2016) 155, doi:10.1140/epjc/s10052-016-3988-x, arXiv:1512.00815.

[31] P. Skands, S. Carrazza, and J. Rojo, "Tuning PYTHIA 8.1: the Monash 2013 Tune", *Eur. Phys. J.* **C74** (2014) 3024, doi:10.1140/epjc/s10052-014-3024-y, arXiv:1404.5630.

[32] G. Busoni et al., "Recommendations on presenting LHC searches for missing transverse energy signals using simplified *s*-channel models of dark matter", arXiv:1603.04156.

[33] S. Ask, "Simulation of Z plus graviton/unparticle production at the LHC", *Eur. Phys. J. C* **60** (2009) 509, doi:10.1140/epjc/s10052-009-0949-7, arXiv:0809.4750.

[34] S. Ask et al., "Real emission and virtual exchange of gravitons and unparticles in PYTHIA8", *Comput. Phys. Commun.* **181** (2010) 1593, doi:10.1016/j.cpc.2010.05.013, arXiv:0912.4233.

[35] R. Corke and T. Sjöstrand, "Interleaved parton showers and tuning prospects", *JHEP* **03** (2011) 032, doi:10.1007/JHEP03(2011)032, arXiv:1011.1759.

[36] P. Nason, "A New method for combining NLO QCD with shower Monte Carlo algorithms", *JHEP* **11** (2004) 040, doi:10.1088/1126-6708/2004/11/040, arXiv:hep-ph/0409146.

[37] S. Frixione, P. Nason, and C. Oleari, "Matching NLO QCD computations with Parton Shower simulations: the POWHEG method", *JHEP* **11** (2007) 070, doi:10.1088/1126-6708/2007/11/070, arXiv:0709.2092.

[38] S. Alioli, P. Nason, C. Oleari, and E. Re, "A general framework for implementing NLO calculations in shower Monte Carlo programs: the POWHEG BOX", *JHEP* **06** (2010) 043, doi:10.1007/JHEP06(2010)043, arXiv:1002.2581.

[39] E. Re, "Single-top Wt-channel production matched with parton showers using the POWHEG method", *Eur. Phys. J. C* **71** (2011) 1547, doi:10.1140/epjc/s10052-011-1547-z, arXiv:1009.2450.

[40] S. Alioli, S.-O. Moch, and P. Uwer, "Hadronic top-quark pair-production with one jet and parton showering", *JHEP* **01** (2012) 137, doi:10.1007/JHEP01(2012)137, arXiv:1110.5251.

[41] J. M. Campbell and R. K. Ellis, "MCFM for the Tevatron and the LHC", *Nucl. Phys. Proc. Suppl.* **205** (2010) 10, doi:10.1016/j.nuclphysbps.2010.08.011, arXiv:1007.3492.

[42] NNPDF Collaboration, "Parton distributions for the LHC Run II", *JHEP* **04** (2015) 040, doi:10.1007/JHEP04(2015)040, arXiv:1410.8849.

[43] GEANT4 Collaboration, "GEANT4—a simulation toolkit", *Nucl. Instrum. Meth. A* **506** (2003) 250, doi:10.1016/S0168-9002(03)01368-8.

[44] J. Allison et al., "Geant4 developments and applications", *IEEE Trans. Nucl. Sci.* **53** (2006) 270, doi:10.1109/TNS.2006.869826.

[45] CMS Collaboration, "Particle-flow event reconstruction in CMS and performance for jets, taus, and $E_{\mathrm{T}}^{\mathrm{miss}}$", CMS Physics Analysis Summary CMS-PAS-PFT-09-001, 2009.

[46] CMS Collaboration, "Commissioning of the particle-flow event with the first LHC collisions recorded in the CMS detector", CMS Physics Analysis Summary CMS-PAS-PFT-10-001, 2010.

[47] CMS Collaboration, "Performance of electron reconstruction and selection with the CMS detector in proton-proton collisions at $\sqrt{s} = 8$ TeV", *JINST* **10** (2015) 06005, doi:10.1088/1748-0221/10/06/P06005, arXiv:1502.02701.

[48] CMS Collaboration, "Performance of CMS muon reconstruction in pp collision events at $\sqrt{s} = 7$ TeV", *JINST* **7** (2012) 10002, doi:10.1088/1748-0221/7/10/P10002, arXiv:1206.4071.

[49] CMS Collaboration, "Reconstruction and identification of τ lepton decays to hadrons and ν_τ at CMS", *JINST* **11** (2016) P01019, doi:10.1088/1748-0221/11/01/P01019, arXiv:1510.07488.

[50] M. Cacciari, G. P. Salam, and G. Soyez, "The anti-k_t jet clustering algorithm", *JHEP* **04** (2008) 063, doi:10.1088/1126-6708/2008/04/063, arXiv:0802.1189.

[51] M. Cacciari, G. P. Salam, and G. Soyez, "FastJet user manual", *Eur. Phys. J. C* **72** (2012) 1896, doi:10.1140/epjc/s10052-012-1896-2, arXiv:1111.6097.

[52] M. Cacciari and G. P. Salam, "Dispelling the N^3 myth for the k_t jet-finder", *Phys. Lett. B* **641** (2006) 57, doi:10.1016/j.physletb.2006.08.037, arXiv:hep-ph/0512210.

[53] CMS Collaboration, "Jet energy scale and resolution in the CMS experiment in pp collisions at 8 TeV", arXiv:1607.03663.

[54] Particle Data Group Collaboration, "Review of Particle Physics", *Chin. Phys.* **C38** (2014) 090001, doi:10.1088/1674-1137/38/9/090001.

[55] CMS Collaboration, "Identification of b-quark jets with the CMS experiment", *JINST* **8** (2013) 04013, doi:10.1088/1748-0221/8/04/P04013, arXiv:1211.4462.

[56] CMS Collaboration, "Performance of b tagging at $\sqrt{s} = 8$ TeV in multijet, ttbar and boosted topology events", CMS Physics Analysis Summary CMS-PAS-BTV-13-001, 2013.

[57] CMS Collaboration, "Identification of b quark jets at the CMS Experiment in the LHC Run 2", CMS Physics Analysis Summary CMS-PAS-BTV-15-001, CERN, Geneva, 2016.

[58] A. Bierweiler, T. Kasprzik, and J. H. Khn, "Vector-boson pair production at the LHC to $\mathcal{O}(\alpha^3)$ accuracy", *JHEP* **12** (2013) 071, doi:10.1007/JHEP12(2013)071, arXiv:1305.5402.

[59] S. Gieseke, T. Kasprzik, and J. H. Kühn, "Vector-boson pair production and electroweak corrections in HERWIG++", *Eur. Phys. J. C* **74** (2014), no. 8, 2988, doi:10.1140/epjc/s10052-014-2988-y, arXiv:1401.3964.

[60] J. Baglio, L. D. Ninh, and M. M. Weber, "Massive gauge boson pair production at the LHC: a next-to-leading order story", *Phys. Rev.* **D88** (2013) 113005, doi:10.1103/PhysRevD.88.113005, arXiv:1307.4331.

[61] CMS Collaboration, "Measurement of the inclusive W and Z production cross sections in pp collisions at $\sqrt{s} = 7$ TeV", *JHEP* **10** (2011) 132, doi:10.1007/JHEP10(2011)132, arXiv:1107.4789.

[62] CMS Collaboration, "CMS Luminosity Measurement for the 2015 Data Taking Period", CMS Physics Analysis Summary CMS-PAS-LUM-15-001, CERN, Geneva, 2016.

[63] CMS Collaboration, "Measurement of the inelastic proton-proton cross section at $\sqrt{s} = 13$ TeV", CMS Physics Analysis Summary CMS-PAS-FSQ-15-005, CERN, Geneva, 2016.

[64] T. Junk, "Confidence level computation for combining searches with small statistics", *Nucl. Instrum. Meth. A* **434** (1999) 435, doi:10.1016/S0168-9002(99)00498-2, arXiv:hep-ex/9902006.

[65] A. L. Read, "Presentation of search results: the CL_s technique", *J. Phys. G* **28** (2002) 2693, doi:10.1088/0954-3899/28/10/313.

[66] G. Cowan, K. Cranmer, E. Gross, and O. Vitells, "Asymptotic formulae for likelihood-based tests of new physics", *Eur. Phys. J. C* **71** (2011) 1554, doi:10.1140/epjc/s10052-011-1554-0, arXiv:1007.1727. [Erratum: doi:10.1140/epjc/s10052-013-2501-z].

[67] ATLAS and CMS Collaborations, LHC Higgs Combination Group, "Procedure for the LHC Higgs boson search combination in Summer 2011", ATL-PHYS-PUB-2011-11, CMS NOTE 2011/005, 2011.

[68] LUX Collaboration, "Improved Limits on Scattering of Weakly Interacting Massive Particles from Reanalysis of 2013 LUX Data", *Phys. Rev. Lett.* **116** (2016) 161301, doi:10.1103/PhysRevLett.116.161301, arXiv:1512.03506.

[69] SuperCDMS Collaboration, "New Results from the Search for Low-Mass Weakly Interacting Massive Particles with the CDMS Low Ionization Threshold Experiment", *Phys. Rev. Lett.* **116** (2016) 071301, doi:10.1103/PhysRevLett.116.071301, arXiv:1509.02448.

[70] PandaX-II Collaboration, "Dark Matter Results from First 98.7-day Data of PandaX-II Experiment", arXiv:1607.07400.

[71] CRESST Collaboration, "Results on light dark matter particles with a low-threshold CRESST-II detector", *Eur. Phys. J.* **C76** (2016) 25, doi:10.1140/epjc/s10052-016-3877-3, arXiv:1509.01515.

[72] Super-Kamiokande Collaboration, "Search for neutrinos from annihilation of captured low-mass dark matter particles in the Sun by Super-Kamiokande", *Phys. Rev. Lett.* **114** (2015), no. 14, 141301, doi:10.1103/PhysRevLett.114.141301, arXiv:1503.04858.

[73] PICO Collaboration, "Improved dark matter search results from PICO-2L Run 2", *Phys. Rev.* **D93** (2016) 061101, doi:10.1103/PhysRevD.93.061101, arXiv:1601.03729.

[74] PICO Collaboration, "Dark matter search results from the PICO-60 CF_3I bubble chamber", *Phys. Rev.* **D93** (2016) 052014, doi:10.1103/PhysRevD.93.052014, arXiv:1510.07754.

[75] IceCube Collaboration, "Improved limits on dark matter annihilation in the Sun with the 79-string IceCube detector and implications for supersymmetry", *JCAP* **04** (2016) 022, doi:10.1088/1475-7516/2016/04/022, arXiv:1601.00653.

[76] S. Kathrein, S. Knapen, and M. J. Strassler, "Bounds from LEP on unparticle interactions with electroweak bosons", *Phys. Rev. D* **84** (2011) 015010, doi:10.1103/PhysRevD.84.015010, arXiv:1012.3737.